Article

Enhanced Mechanical and Self-Healing Properties of Carbon Fiber-Reinforced Epoxy Laminates Using In Situ-Grown ZnO Nanorods and Thermo-Reversible Bonds

Poulami Banerjee,[†] Sampath Parasuram,[†] Subodh Kumar, and Suryasarathi Bose*

Read Online

ACCESS | Metrics & More | Article Recommendations | SI Supporting Information

ABSTRACT: Advanced hierarchical carbon fiber epoxy laminates with an engineered interface using in situ-grown ZnO nanorods on carbon fiber resulted in strong mechanical interlocking with the matrix. To further strengthen the interface, "site-specific" modification was realized by modifying the ZnO nanorods with bismaleimide (BMI), which facilitates "thermo-reversible" bonds with graphene oxide (GO) present in the matrix. The resulting laminates exhibited an improvement in flexural strength by 20% and in interlaminar shear strength (ILSS) by 28%. In order to gain a mechanistic insight, few laminates were prepared by "non-selectively" modifying the ZnO-grown carbon fiber (CF) with BMI. The "nonselectively" modified laminates showed flexural strength and ILSS improvement by 43 and 39%, respectively. The "nonselective" modification resulted in a strong improvement in mechanical properties; however, the "site-specific" modification yielded a higher self-healing efficiency (81%). Raman spectroscopy, scanning electron microscopy (SEM) micrographs, atomic force microscope (AFM) analysis, and contact angle analysis indicated a strong interaction of the modified CFs with the resin. Enhanced surface area and energy, along with a decrease in segmental molecular mobility observed from dynamic mechanical analysis, confirmed the mechanism for a better performance. Microscopic images revealed an improved interfacial behavior of the fractured samples, indicating a higher interfacial adhesion in the modified laminates. Besides mechanical properties, these laminates also showed excellent electromagnetic interference (EMI) shielding performance. The laminates with only ZnO-modified CF showed a high shielding effectiveness of −47 dB.
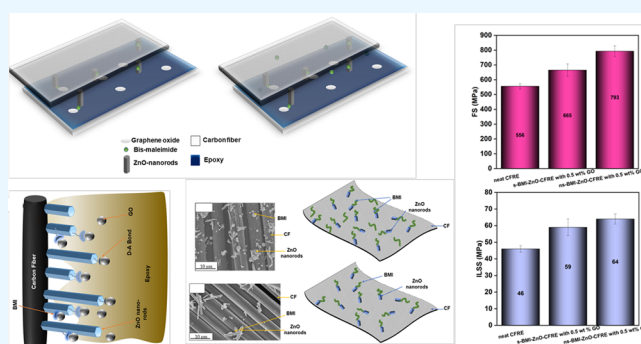
1. INTRODUCTION

Carbon fiber-reinforced epoxy (CFRE) laminates have been established as suitable materials for the automotive and aerospace industries because of their unique and unparalleled structural properties.[1−5] However, there are continued efforts to improve the properties and durability of these laminates.[6−8] The main focus is strengthening the interface between the epoxy matrix and carbon fiber (CF) interface to prevent failure and also exploring the possibility of reformation of debonded sites at the interface after failure.[9−13] Furthermore, the modification of interfaces in such CFRE laminates for aerospace applications also demands stringent EM interference requirements during aircraft flight.[14−16]

Until now, the fabrication of hierarchical fiber-modified advanced laminates was met with limitations affecting the inherent fiber structural integrity and was reflected in mechanical properties.[17−20] While treatments such as polymeric sizing, matrix modification, and fiber−particle interaction for an enhanced fiber−matrix interface have been widely researched on, the synergistic improvement on in-plane and out-of-plane properties has not been easily achieved.[17−23]

Furthermore, research on interface reformation postmaterial failure is a domain not well understood yet.

In our previous works, we established a thermo-reversible linkage at the interface of CF−epoxy using bismaleimide (BMI) and graphene oxide (GO) to form a Diels−Alder (DA) adduct.[24] We observed an improvement in both flexural strength (FS) and interlaminar shear strength (ILSS) values of the resultant laminates. Furthermore, post the self-healing cycle, strength recovery in terms of ILSS values of about 70% was observed. We also developed in situ-grown ZnO nanorod-modified CFs to improve the interface through mechanical interlocking.[25] Two separate laminates were fabricated in this case, one with 10 layers of ZnO−CF and the other with 5 alternate layers of ZnO−CF and BMI−CF. In both cases,
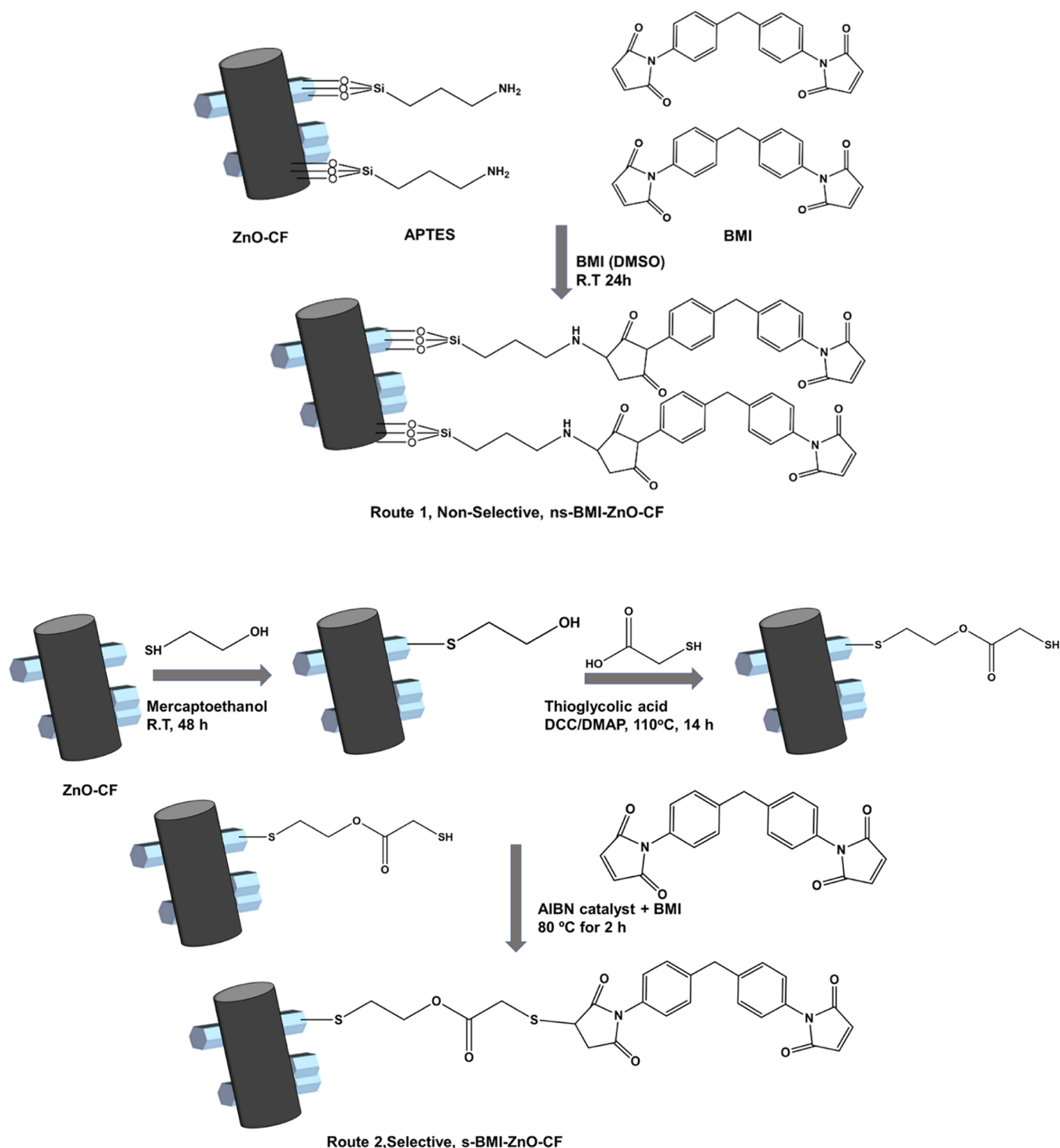
Figure 1. Chemical routes to attach BMI on ZnO−CF. Route 1 indicates nonselective deposition and route 2 indicates selective deposition of BMI.

mechanical property enhancement and considerable strength recovery in ILSS post self-healing in the latter case were achieved. What was observed from this is that a combination of chemically bonded and mechanically interlocked interfaces led to an improvement in strength while also allowing for substantial self-healing at the interface.

In the present work, we explore more extensively the idea of depositing the dienophile BMI directly over the in situ-grown ZnO nanorods on the surface of the CF mat (ZnO−CF). We hypothesize that the presence of BMI over the surface of ZnO rods shall not only increase the surface area of the CF mat but

also interact with GO present in the subsurface or bulk of the epoxy matrix, leading to a greater number of DA bonds. With this aim, we fabricated 10-layered advanced hierarchical CFRE laminates of two types. In the first type, each ZNO−CF mat was subjected to "nonselective" deposition of BMI, i.e., BMI will be attached to both ZnO nanorods and CF. In the second type, "site-selective" deposition of BMI only over the ZnO nanorods in the ZnO−CF mat was achieved. The chemical modifications over the CFs were obtained through the optimized dip-coating method. A range of characterization techniques was used to confirm the presence of modified
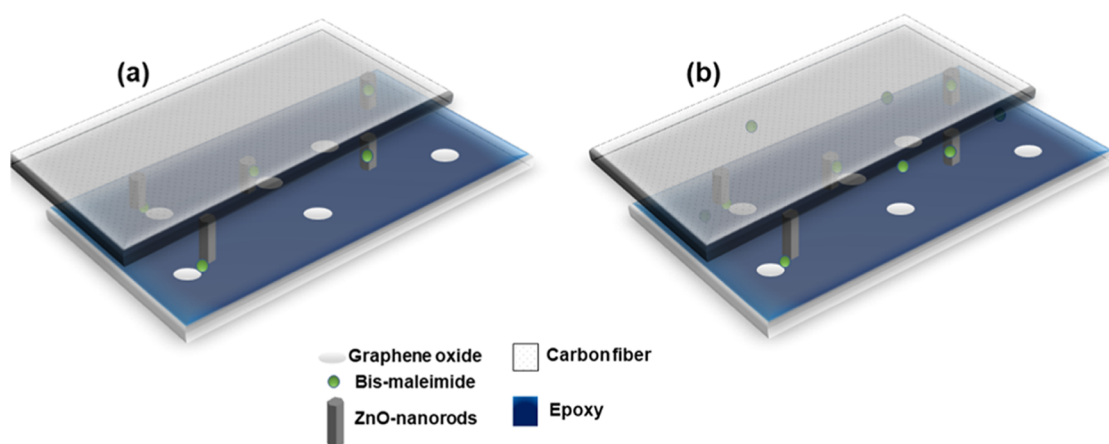
Figure 2. Design of the hybrid 10-layered laminates fabricated for (a) s-BMI-ZnO−CFRE and (b) ns-BMI-ZnO−CFRE, respectively, with 0.5 wt % GO dispersed in epoxy.

fibers, and micrographic evidence showed the differences in the nonselective and selective deposition of bismaleimide, respectively. Mechanical properties were evaluated in terms of FS and ILSS, as well as dynamic mechanical analysis (DMA). The work involves, for the first time, the generation of a synergistic improvement in mechanical strength and self-healing properties on a 10-layered advanced CFRE laminate that can be easily translated into industrial applications. Until now, no other literature to our knowledge has been able to achieve a combination of (1) improved in-plane and out-of-plane properties and (2) self-healing efficiency in a macroscopic carbon fiber laminate. To the best of our knowledge, such a detailed analysis of a multiphase system consisting of CF modified with an organic molecule (BMI) and a ceramic nanorod (ZnO) to provide improved interfacial interactions with the GO-modified epoxy matrix has not been attempted in the past. We believe that such a hybrid system can be translated to industrial applications with ease and improves the efficient durability of aircraft structures.

2. MATERIALS AND METHODOLOGY

2.1. Materials. A bidirectional CF mat with a GSM 200 and filament diameter of 7 μm was purchased from Bhor Chemicals. Diglycidyl ether of bisphenol A (DGEBA) epoxy prepolymer with an amine-based hardener system was purchased from Atul Industries. Zinc acetate (ZnAc), zinc nitrate (ZnNO$_3$·6H$_2$O), and hexamethylenetetramine (HMTA) were obtained from Sigma-Aldrich. Graphene oxide (GO) was obtained from BT Corp. 1,1-(Methylenedi-4,1-phenylene)bismaleimide (BMI) (95% pure) was obtained from Sigma-Aldrich. Hydrogen peroxide solution (H$_2$O$_2$, 30% w/v) was obtained from Qualigens. γ-aminopropyltriethoxysilane (APTES), purchased from Sigma-Aldrich, was used as the amino-functional coupling agent. AR-grade N,N-dimethylformamide (DMF), purchased from SDFCL, was used as the solvent for BMI. Mercaptoethanol was purchased from Sigma-Aldrich. Thioglycolic acid (TGA) was used for esterification with N,N'-dicyclohexylcarbodiimide (DCC)/4-dimethylaminopyridine (DMAP) as a catalyst, all purchased from Sigma-Aldrich. Site-selective deposition of BMI was attained using AIBN purchased from Sigma-Aldrich as a catalyst in a DMF solvent. Acetone, ethanol, toluene, and deionized water used as solvents were purchased from commercial sources. Raw

materials for vacuum-assisted resin transfer molding (VARTM) were purchased from Amtek International.

2.2. Processing. *2.2.1. Site-Nonselective Deposition of BMI over ZnO−CF.* ZnO nanorods on CF were grown using the method described in our previous work, and the resulting mat is referred to as ZnO−CF.[25] Briefly, a uniform ZnO nanorod deposition on the surface of CFs was achieved using the successive ionic layer adsorption and reaction (SILAR) technique. The CF mat was dipped in 10 mmol of zinc acetate (ZnAc) aqueous solution prepared through a stirring and sonication process to obtain the ZnO seed layer. Following this, the growth of ZnO nanorods was accomplished by immersing the CF mat in an aqueous solution containing 20 mmol of zinc nitrate (ZnNO$_3$·6H$_2$O) and 20 mmol of hexamethylenetetramine (HMTA) and subjecting them to heating at 90 °C for 4 h. BMI was deposited on ZnO−CF via a two-step process. ZnO−CF was functionalized with 1 wt % APTES at 80 °C for 2 h in 100 mL of DMSO solvent. Then, the APTES-functionalized ZnO−CF was immersed in the BMI (DMSO) solution (5 wt % wrt ZnO−CF) and placed at room temperature for 24 h. The resulting fiber mat was washed and dried with DI water and acetone repeatedly. Here, BMI is expected to be attached with both ZnO nanorods and CF since APTES treatment is through an adsorption process and the aminopropyl groups can anchor on any oxygen-containing surface without selectivity, and the resulting mat is referred to as ns-BMI-ZnO−CF.[26]

2.2.2. Site-Selective Deposition of BMI over ZnO−CF. Here, ZnO−CF was reacted with 1 wt % mercaptoethanol and kept at room temperature for 48 h. Then, the modified mat was subjected to esterification via thioglycolic acid using 0.1−1 wt % DCC/DMAP as the catalyst at 110 °C for 14 h. Finally, the mat was immersed in 5 wt % BMI (w.r.t. ZnO−CF) solution with 0.01 wt % AIBN catalyst at 80 °C for 2 h for a 'thiol−ene' prospective click reaction.[27] Here, BMI is expected to be attached only with ZnO nanorods because of the selective affinity of thiol (−SH) groups toward metal surfaces forming dative bonds, and the resulting mat is referred to as s-BMI-ZnO−CF. The sequential reaction is conducted to avoid degrading the structural integrity of CF mats. The −SH reaction with Zn^{2+} allows for the dangling −OH chains to react with TGA. Figure 1 illustrates the chemical route of the deposition of BMI over ZnO−CF.

2.2.3. Fabrication of Laminates. Two laminates were fabricated via the VARTM technique.[28,29] The fibers were stacked one above the other on a glass mold sandwiched between the release film and peel ply. A resin infusion mesh was placed on the top surface, allowing the epoxy resin to flow and distribute throughout the fibers. The vacuum bag was placed above the setup, creating a pressure gradient driving the resin to impregnate the fibers. The epoxy resin-hardener in a predefined ratio was infused into the vacuum bag through the inlet line connected with the resin tank. Once the composite developed sufficient dimensional stability, it was removed from the mold and postcured to complete the cross-linking reaction. The entire setup was prepared manually in the laboratory setting.

The first laminate contained 10 layers of nonsite-selective modified carbon fibers referred to as ns-BMI-ZnO–CFRE with 0.5 wt % GO and the second one contained 10 layers of site-selective modified carbon fibers referred to as s-BMI-ZnO–CFRE with 0.5 wt % GO, as depicted in Figure 2. In both cases, 0.5 wt % GO was dispersed in epoxy via stirring and sonication. GO not only acted as a reinforcement to the matrix because of its solution compatibility with epoxy but also served as a diene because of the presence of a 1,2-butadiene structure on the edge of GO and a *cis*-3,5-cyclohexadiene-1,2-diol structure present on the surface, thus forming DA bonds with BMI.[30,31] To assess the improvement in mechanical properties and self-healing of the modified laminates, neat CFREs (unmodified CFs and neat epoxy without any GO) were used as the control samples.

Epoxy and polyamine hardeners were mixed in a ratio of 100:24 and 0.5 wt % GO was dispersed or not dispersed into it, depending on the case. It was then infused into the neat or modified fibers, depending on the case, in a VARTM setup. This was followed by curing at 80 °C and postcuring at 100, 120, and 150 °C through a step-up process. The cured laminates were then furnace-cooled to room temperature. The nomenclature used for various laminates is listed in Table 1.

Table 1. Nomenclature Used for Various Laminates

abbreviation	description
neat CFRE	unmodified carbon fiber-reinforced epoxy
ns-BMI-ZnO–CFRE with 0.5 wt % GO	10 layers of ZnO–CF with nonselectively deposited BMI forming a laminate with 0.5 wt % GO dispersed in epoxy
s-BMI-ZnO–CFRE with 0.5 wt % GO	10 layers of ZnO–CF with selectively deposited BMI forming a laminate with 0.5 wt % GO dispersed in epoxy
ZnO–CFRE with 0.5 wt % GO	10 layers of ZnO–CF forming a laminate with 0.5 wt % GO dispersed in epoxy

3. CHARACTERIZATION TECHNIQUES

Microscopic imaging of BMI's nonselective and selective deposition over ZnO–CF was conducted using scanning electron microscopy (SEM) equipped with energy-dispersive X-ray spectroscopy (EDS) analysis. Surface roughness and the contact angle of the fiber–matrix interface play significant roles in resin wetting characteristics. Thus, the neat and modified fibers' surface roughness was measured using an atomic force microscope (AFM) in the noncontact mode. The fibers were rigidly extended, glued on a support, and observed with a PARK NX-10 microscope. The cylindrical piezo transducer allowed the observation of a $10 \times 10 \ \mu m^2$ sample surface with

2 μm vertical corrugations. Raman spectroscopy was also conducted to determine the ratio of ordered and disordered bonds on the neat, ns-CF, and s-CF surfaces. Raman spectra for the CFs were recorded on a WITec system with a 532 nm excitation wavelength. With the analysis of the intensity ratio of the peaks at around 1350 cm^{-1} (D band) and 1595 cm^{-1} (G band), respectively, the structural uniformity and aberrations of the sample were determined.

Furthermore, surface energy analysis provides an additional input on the affinity for the matrix to wet the fibers.[32−34] Therefore, surface energy analysis on the neat and modified fibers was conducted by using deionized water as the polar solvent and diiodomethane as the organic solvent. The polar and dispersive components of the surface energy were calculated by using the Owens, Wendt, Rabel, and Kaelble's (OWRK) method.

Dynamic mechanical analysis was conducted to determine the elastic modulus, loss modulus, and Tg.

Flexural strength (FS) and interlaminar shear strength (ILSS) tests of the unmodified and modified laminates were conducted on a ZEISS UTM machine with a load cell of 10 kN and a cross-head velocity of 1 mm/min. Around 6 specimens for FS tests and 10 samples for ILSS tests were machined out from each of the fabricated laminates following ASTM D7264/D7264M-07 and ASTM D2344/D, respectively. A preload of 2−5 N was applied.

FS was calculated from the equation

$$\sigma = \frac{3PL}{2bh^2} \tag{1}$$

And ILSS was calculated from the equation

$$\sigma = \frac{3P}{4bh} \tag{2}$$

Samples after ILSS tests were placed in an oven and heated at 60 °C for 24 h, followed by slow cooling to room temperature. Following this, ILSS tests were further performed on the samples. The self-healing efficiency was calculated as

$$\%S. \ H. = \frac{P_f}{P_i} \times 100\% \tag{3}$$

where P_i and P_f are the peak loads on the samples measured in ILSS tests before and after self-healing, respectively.

EMI shielding interference was studied using the Keysight FieldFox microwave analyzer N9918A in the frequency range of 8.2−12.4 GHz. S-parameters (S_{11}, S_{12}, S_{21}, S_{22}) were obtained from a vector network analyzer (VNA), which were then used to obtain the SE$_T$ and shielding effectiveness due to reflection (SE$_R$) and absorption (SE$_A$). The sample thickness for all of the CFRE systems was 2.2 mm.

4. RESULTS AND DISCUSSION

4.1. Microstructural Characterization by SEM. The SEM micrograph of ns-BMI-ZnO–CF is presented in Figure 3(a), shown schematically in Figure 3(c), indicating the growth of ZnO nanorods on the surface of CFs and BMI covalently anchored both on CFs and ZnO. This "nonselective" deposition panned across the CF mat without forming a BMI film between the tows. The SEM micrograph of s-BMI-ZnO–CF is presented in Figure 3(d), shown schematically in Figure 3(f), indicating the affinity of BMI molecules
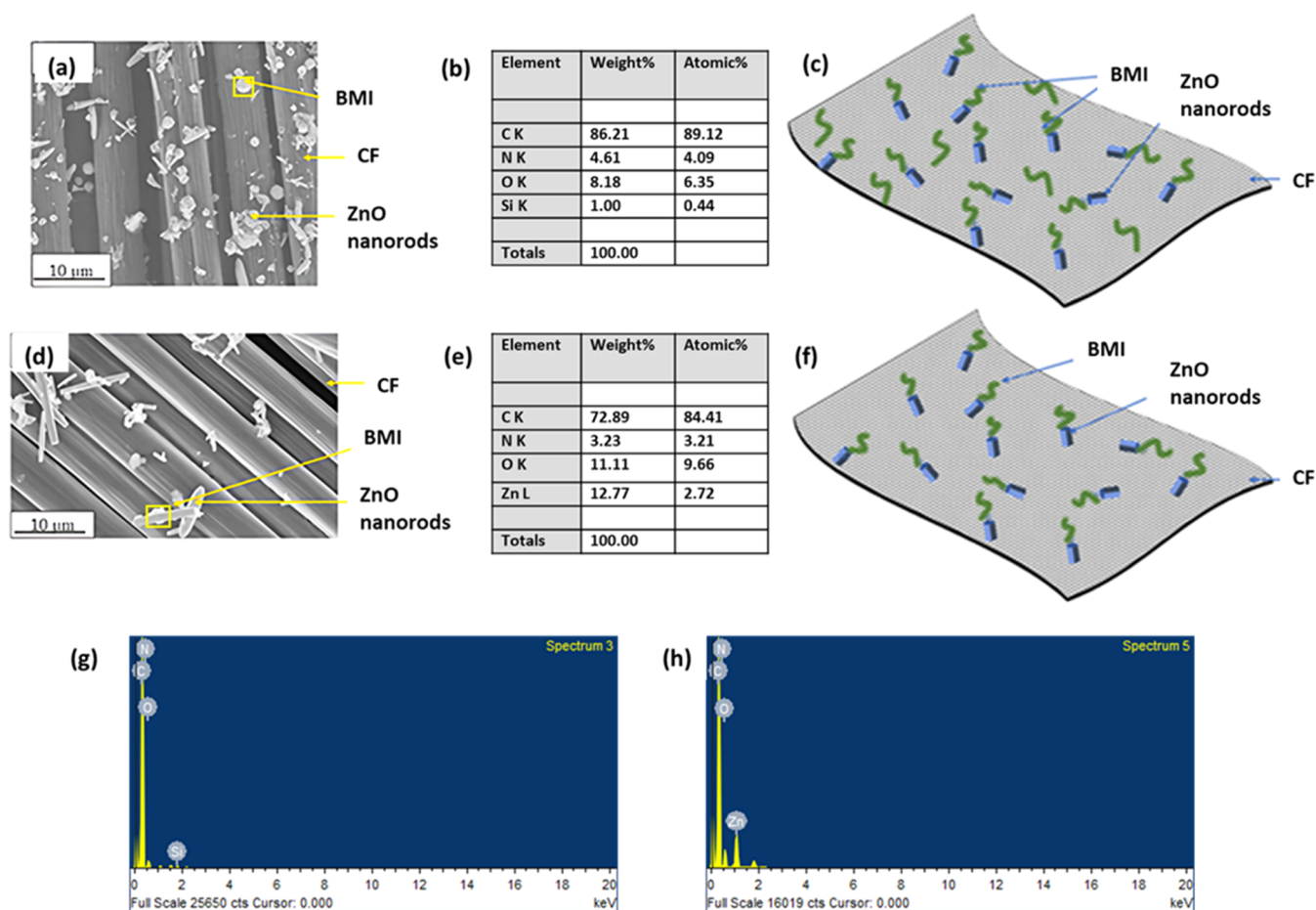
Figure 3. (a) SEM micrograph, (b) EDS elemental analysis table of the highlighted square feature, and (c) representational schematic of ns-CF; (d) SEM micrograph, (e) EDS elemental analysis table of the highlighted square feature, and (f) representational schematic of s-CF; (g) EDS analysis spectrum of the highlighted square feature in ns-CF; and (h) EDS analysis spectrum of the highlighted square feature in s-CF.

"selectively" toward ZnO nanorods with hardly any deposition over CFs.

The EDS elemental analysis table of the highlighted square feature in ns-CF is presented in Figure 3(b), and the EDS spectrum in Figure 3(g) indicates the presence of C, N, O, and Si elements. The trace amount of Si comes from the APTES used in the nonselective deposition of BMI over ZnO−CF. The location for EDS was specifically selected away from ZnO nanorods to show the nonselective deposition of BMI on the CF surface. Figure 3(e) presents the EDS elemental analysis table of the highlighted square feature in s-CF, and the EDS spectrum in Figure 3(h) shows the presence of C, N, O, and Zn.[24,25] Thus, the SEM micrographs, along with the EDS analysis data, confirm that while the amination route led to a nonselective deposition of BMI over ZnO−CF, the thiol−ene click reaction route led to an elective deposition over ZnO−CF. As reported in our previous work, FTIR analysis confirmed the characteristic peaks indicating the presence of BMI over the CF surface.[24]

4.2. Raman Spectroscopy. Raman spectroscopy analysis was conducted on the neat and modified CFs to assess the crystallites and the disordered parts over the surface of the CFs. Raman spectra of carbonaceous materials, such as CFs, CNTs, graphene, GO, etc., consist of several wavenumber bands. However, two major characteristic bands are used to assess the nature of the modification of CFs. The 1595 cm^{-1} band (G band) is assigned to the E_{2g} vibrational mode of the graphitic crystal, which is present in all graphitic structures. The Raman band at ∼1330 cm^{-1} is associated with the boundaries of the graphitic crystals and is related to structural disorder effects. This band is visible in the case of poorly graphitized fibers.[35−38]

Raman spectra of neat CF, ns-BMI-ZnO−CF, and s-BMI-ZnO−CF are reported in Figure 4. While neat CF has an I_D/I_G value of 1.03, ns-BMI-ZnO−CF and s-BMI-ZnO−CF have values of 1.10 and 1.14, respectively. A higher I_D/I_G ratio indicates that the sp^2 bonds of the graphitized crystals were broken due to the chemical treatment on the surface of the CFs and had transitioned to sp^3 hybridization. Higher disordered sites over the surface of the modified CFs could indicate more active regions leading to a better interaction of the modified CFs with the matrix, thereby improving the matrix adhesion over the CFs. Furthermore, the rise in disordered sites also indicates an increase in surface roughness of the CFs leading to a higher surface area for better matrix adhesion.[39,40]

4.3. Surface Roughness and Surface Energy Analysis. The AFM images of the surfaces of neat and modified CFs shown in Figure 5(a−c) indicate an increase in the average roughness. While neat CF had a R_a value of 0.5 μm, s-BMI-ZnO−CF, and ns-BMI-ZnO−CF exhibited R_a values of 2.3 and 3.5 μm, respectively. The R_a value of ns-BMI-ZnO−CF is higher than that of s-BMI-ZnO−CF because of the deposition of BMI over a large area. The higher surface roughness of
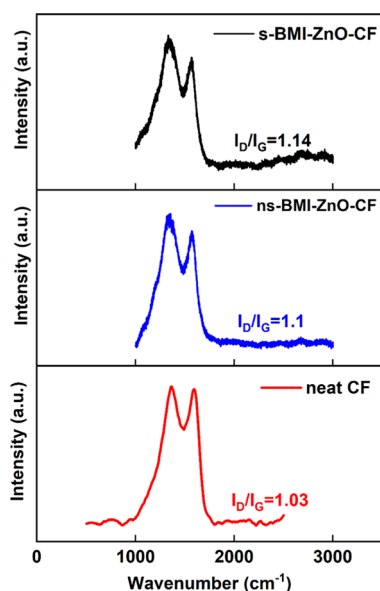
Figure 4. Raman spectra depicting the I_D/I_G ratios of neat CF, ns-BMI-ZnO−CF, and s-BMI-ZnO−CF.

modified CFs should result in their better wettability and interfacial adhesion with the epoxy matrix.[41−43]

The surface energy components of ZnO−CF, ns-BMI-ZnO−CF, and s-BMI-ZnO−CF shown in Figure 5(d) were calculated using the Bruscher's method. The total surface energy is divided into polar and dispersive components.

$$\gamma_T = \gamma_P + \gamma_d \qquad (4)$$

While the polar component of the surface energy (γ_P) is an indication of the presence of polar functional groups and unsaturated carbon atoms exposed on the surface, the dispersive element (γ_d) characterizes the intrinsic structure of the graphite crystal.

The total surface energy for ns-BMI-ZnO−CF and s-BMI-ZnO−CF was observed to be higher than that of ZnO−CF by 17 and 15%, respectively. A higher surface energy indicates better adhesion of the CFs with the matrix and an improved interfacial strength.[44]

4.4. Mechanical Properties. The modification at each lamina on the overall bending properties of the hierarchical laminates was observed by the performance of the FS and ILSS of the samples machined from the laminates. The tests were
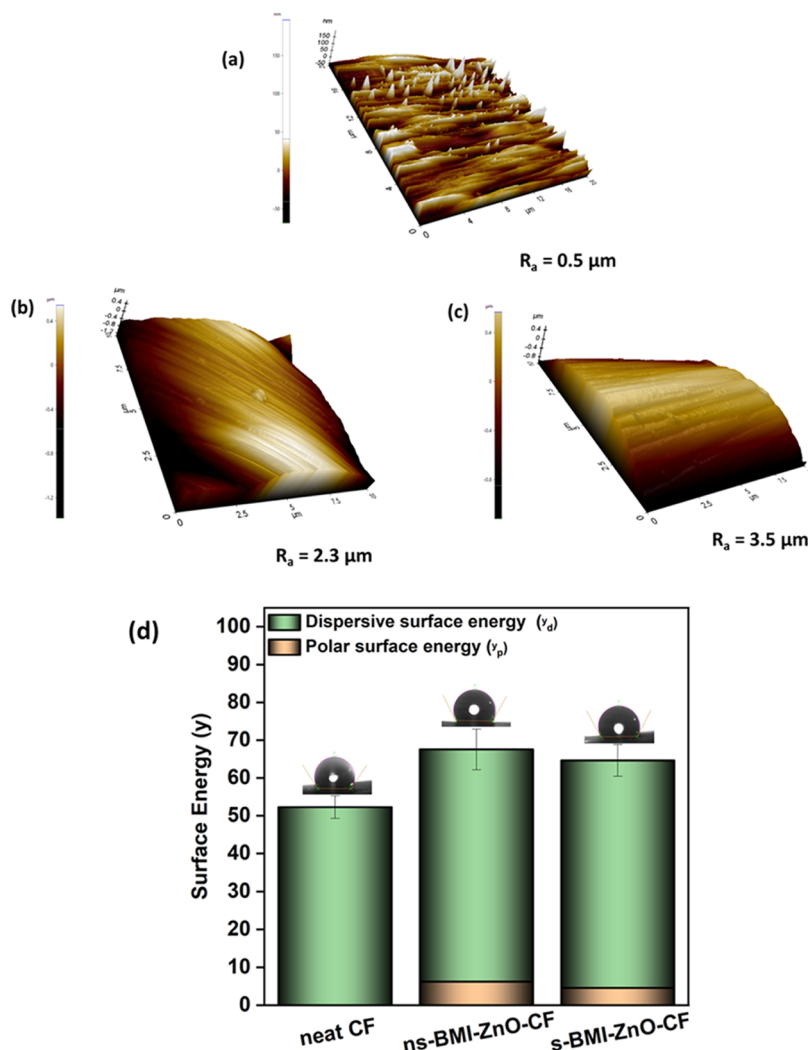

Figure 5. AFM images depicting the surface roughness R_a values of (a) ZnO−CF, (b) s-BMI-ZnO−CF, and (c) ns-BMI-ZnO−CF. (d) Bar diagram showing the surface energy components of neat CF, s-BMI-ZnO−CF, and ns-BMI-ZnO−CF.
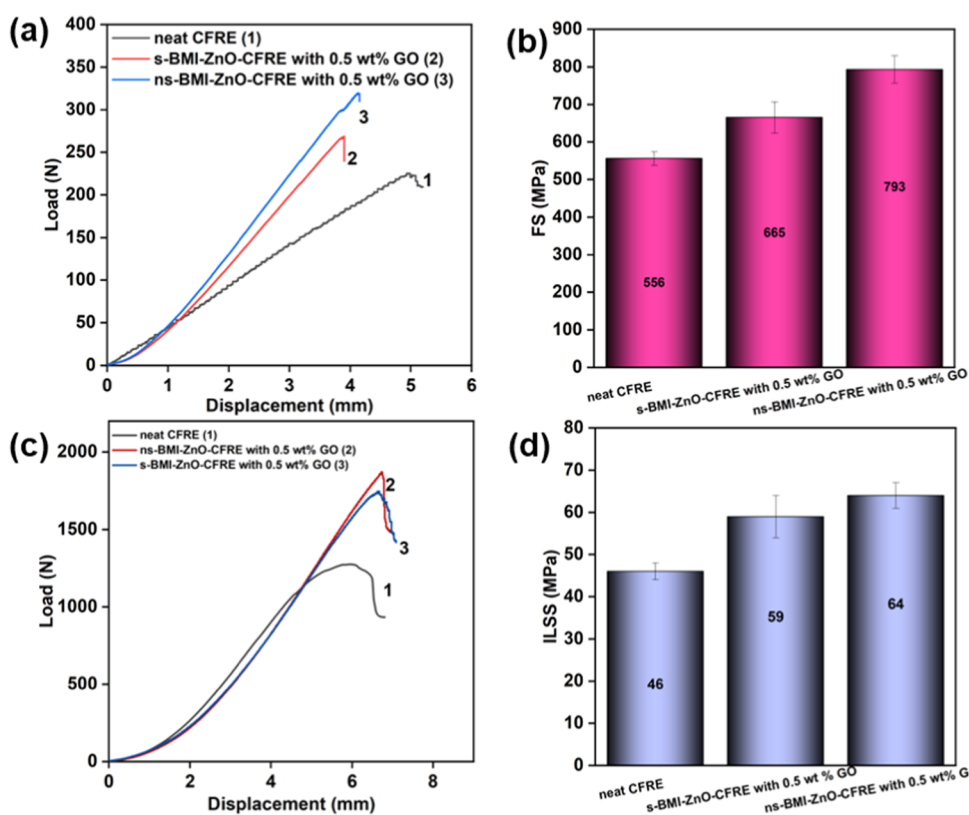
Figure 6. (a) Load−displacement curves for FS tests and (b) FS values of neat CFRE, s-BMI-ZnO−CFRE with 0.5 wt % GO, and ns-BMI-ZnO−CFRE with 0.5 wt % GO. (c) Load−displacement curves for ILSS tests and (d) ILSS values of neat CFRE, s-BMI-ZnO−CFRE with 0.5 wt % GO, and ns-BMI-ZnO−CFRE with 0.5 wt % GO.

chosen to replicate the dominant loads on aircraft wings during takeoff and landing.

The modified laminates are ns-BMI-ZnO−CFRE with 0.5 wt % GO and s-BMI-ZnO−CFRE with 0.5 wt % GO, respectively. In ns-BMI-ZnO−CFRE, BMI was nonselectively deposited on ZnO−CF mats in all of the 10 layers. In s-BMI-ZnO−CFRE, BMI was selectively deposited on ZnO−CF mats in all of the 10 layers. The epoxy resin had 0.5 wt % GO dispersed in it in both the cases. The laminates were fabricated by the VARTM technique.

The load versus displacement curves for flexural tests are shown in Figure 6(a), and the FS values obtained from these are shown in Figure 6(b). FS of neat CFRE is 556 ± 18 MPa. FS of s-BMI-ZnO−CFRE with 0.5 wt % GO shows an increase of 20% to 665 ± 42 MPa. FS of ns-BMI-ZnO−CFRE with 0.5 wt % GO shows an even higher increase of 43% to 793 ± 36 MPa.

The load versus displacement curves for ILSS tests are shown in Figure 6(c), and the ILSS values obtained from these are shown in Figure 6(d). ILSS values exhibit a similar trend. Neat CFRE has an ILSS value of 46 ± 2 MPa. ILSS of s-BMI-ZnO−CFRE with 0.5 wt % GO shows an increase of 28% to 59 ± 5 MPa. ILSS of ns-BMI-ZnO−CFRE with 0.5 wt % GO shows an even higher increase by 39% to 64 ± 3 MPa.

The increase in mechanical properties with the modification of CFRE laminates can be attributed to a few primary strengthening mechanisms. First, the dispersion of 0.5 wt % GO in the epoxy matrix improves the matrix-dominated mechanical properties. Next, in situ-grown ZnO hexagonal rods increase the surface area and mechanical impingement into the epoxy matrix. Furthermore, BMI present on ZnO and

CF makes DA bonds with the GO present in the epoxy near the fiber−matrix interface.

There are two plausible reasons for the greater increase in mechanical properties of ns-BMI-ZnO−CFRE than s-BMI-ZnO−CFRE with 0.5 wt % GO. First, the route of the thiol−ene click reaction for the establishment of selective deposition of BMI over the ZnO nanorods is a harsher chemical treatment, which might have caused some damage to CFs, reducing their strength in the case of s-CFRE. Second, BMI is present over both ZnO nanorods as well as CFs making a larger number of DA bonds, giving rise to a higher interfacial strength in the case of ns-BMI-ZnO−CFRE.

4.5. Self-Healing. The failure mode for the flexural samples was through the "crushing mode", while ILSS samples failed by the "sliding mode".[45−48] Therefore, strength recovery analysis was performed on the ILSS samples of s-BMI-ZnO−CFRE with 0.5 wt % GO and ns-BMI-ZnO−CFRE with 0.5 wt % GO, respectively. The failed ILSS samples were kept in an oven at 60 °C for 24 h, followed by oven cooling for self-healing. The samples were tested again in the UTM to gauge the recovery of strength post failure. Figure 7(a) shows the load−displacement curves, and Figure 7(b) shows the ILSS values before and after self-healing for s-BMI-ZnO−CFRE with 0.5 wt % GO. Figure 7(c) shows the load−displacement curves, and Figure 7(d) shows the ILSS values before and after self-healing for ns-BMI-ZnO−CFRE with 0.5 wt % GO. It is observed that the self-healing efficiency for s-BMI-ZnO−CFRE with 0.5 wt % GO is 81%, while that for ns-BMI-ZnO−CFRE with 0.5 wt % GO is 73%. This indicates the thermo-reversible rejoining of debonded sites at the interface during self-healing.
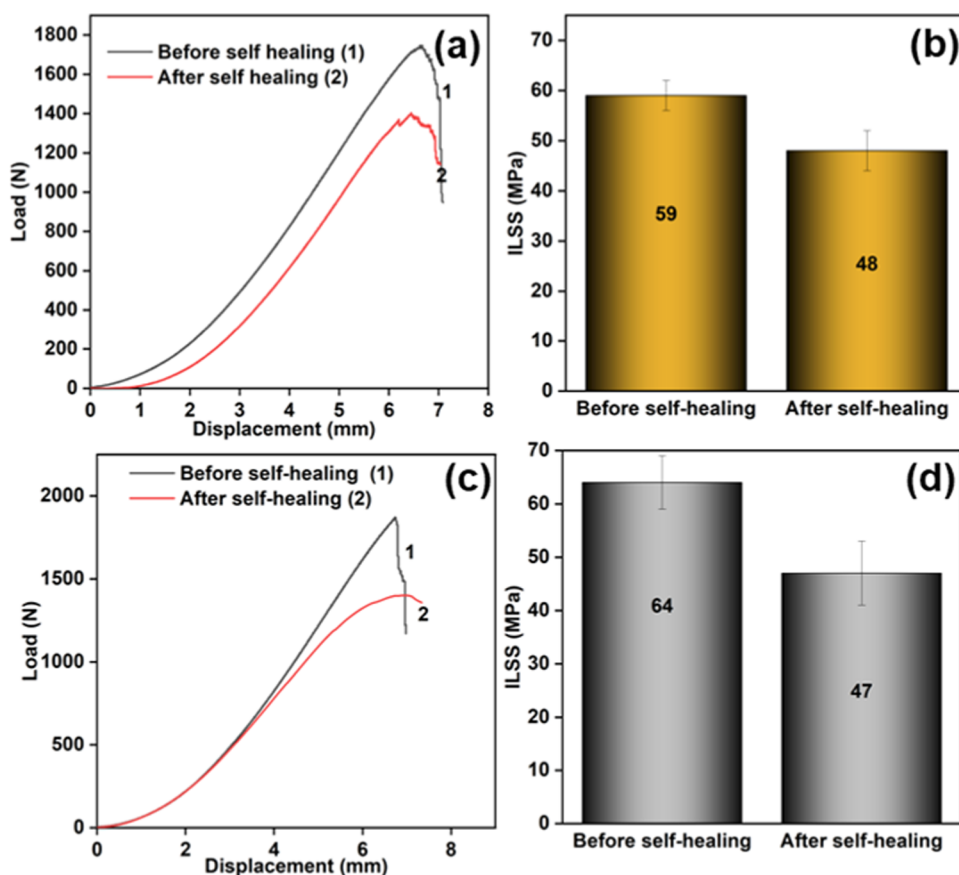
Figure 7. (a) Load−displacement curves and (b) ILSS values for s-BMI-ZnO−CFRE with 0.5 wt % GO before and after the self-healing cycle. (c) Load−displacement curves and (d) ILSS values for ns-BMI-ZnO−CFRE with 0.5 wt % GO before and after the self-healing cycle.

Evidence of DA bond formation has been presented in our previous work.[25]

4.6. Dynamic Mechanical Analysis. Dynamic mechanical analysis of the neat and modified CFREs was performed to analyze the dynamic elastic modulus and glass transition temperature. Several earlier reports have demonstrated a strong connection between the molecular behavior and its correlation with the mechanical performance of polymer composites.[49,50]

Figure 8 shows the variation of storage modulus of neat CFRE, s-BMI-ZnO−CFRE with 0.5 wt % GO, and ns-BMI-ZnO−CFRE with 0.5 wt % GO with temperature. Storage modulus does not change up to a certain temperature, followed by a steep drop showing the transition to the viscous region of the epoxy polymer caused by energy dissipation from the polymer chain movements. Both the modified laminates had similar initial storage modulus values, about 22% higher than neat CFRE. The increased rigidity of the modified laminates could be attributed to the fiber modifications that fill the spaces and cement the warp and weft threads together. The mechanical behavior of the yarns is changed, and the relative rotation of the yarns at interlacing is inhibited.[51,52] However, the drop in storage modulus occurred at about 121 °C for neat CFRE, at about 85 °C for ns-BMI-ZnO−CFRE with 0.5 wt % GO, and at about 81 °C for s-BMI-ZnO−CFRE with 0.5 wt % GO.

Loss modulus depicts the energy dissipated as heat when the material turns viscous. In Figure S1(a), it is observed that the initial loss modulus of neat CFRE was lower than that of ns-BMI-ZnO−CFRE with 0.5 wt % GO, which was, in turn, lower
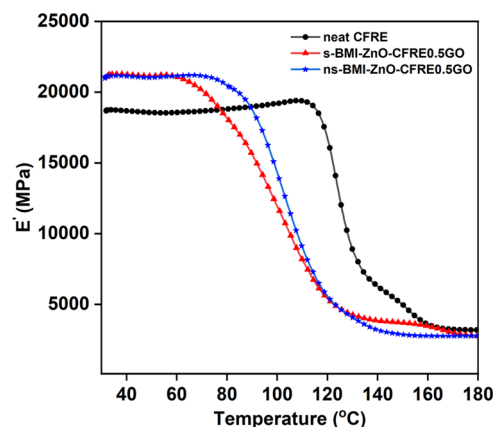

Figure 8. Variation of storage modulus with temperature for neat CFRE, ns-BMI-ZnO−CFRE with 0.5 wt % GO, and s-BMI-ZnO−CFRE with 0.5 wt % GO.

than that of s-BMI-ZnO−CFRE with 0.5 wt % GO. However, the loss modulus peaks of neat CFRE, ns-BMI-ZnO−CFRE with 0.5 wt % GO, and s-BMI-ZnO−CFRE with 0.5 wt % GO are obtained at 123, 100, and 72 °C, respectively. This implies that molecular friction of the modified CFRE laminates increases at a lower temperature than in the neat CFRE laminate; i.e., the viscous state for the hierarchical laminates is reached at lower temperatures.

The damping factor (tan δ) in Figure S1b is used to define the glass transition temperature (T_g) of the laminates. The tan δ curve's first peak represents the system's Tg. The Tgs for

neat CFRE, ns-BMI-ZnO−CFRE with 0.5 wt % GO, and s-CFRE with 0.5 wt % GO are attained at 130, 117, and 88 °C, respectively.

The onset of a drop in the storage modulus curve is also a measure of the glass transition temperature (T_g) of the laminates. Obtaining the Tg from storage modulus curves is particularly helpful as it gives a reliable indication of when the material's mechanical strength starts to degrade with temperature and is particularly useful in establishing the service range for load-bearing components. The Tgs for neat CFRE, ns-BMI-ZnO−CFRE with 0.5 wt % GO, and s-CFRE with 0.5 wt % GO are attained at 121, 85, and 81 °C, respectively. The storage modulus trend is a typical indicator of fiber and matrix modification that led to reaching the viscoelastic peak earlier than the neat laminates. This implies that the polymeric chain motion started at a much lower temperature for the modified CFRE laminates than for the neat CFRE laminates. This could be an indication of the self-healing temperature of the hierarchical laminates. At around 60 °C, modifications made on the laminates interacted with the polymeric chains and led to a segmental motion, allowing for chemical interactions at the interface. Since the laminates are still in their elastic regime, degradation of mechanical properties does not occur at around this temperature. Still, a higher molecular mobility could be a significant cause of the effective self-healing efficiency.

4.7. SEM Fractography. Fractured surfaces of the neat and modified CFREs were examined under SEM to determine the interface between the fibers and the matrix and the extent of matrix adhesion on the fiber surfaces. It is observed in Figure 9(a) that while the neat CFRE appeared to have less
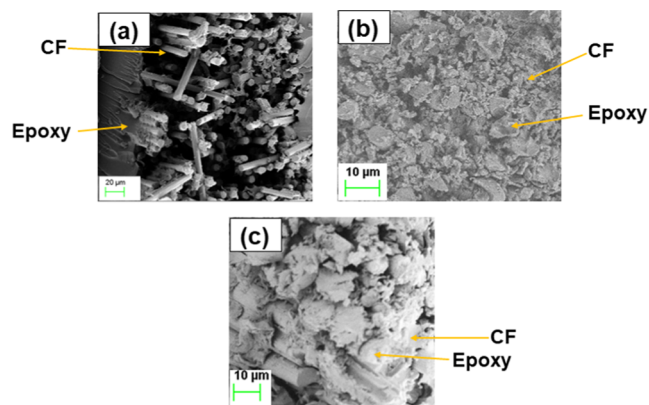

Figure 9. SEM fractographs of the fractured surface of (a) neat CFRE, (b) ns-BMI-ZnO−CFRE with 0.5 wt % GO, and (c) s-BMI-ZnO−CFRE with 0.5 wt % GO.

matrix adhesion, both ns-BMI-ZnO−CFRE with 0.5 wt % GO and s-BMI-ZnO−CFRE with 0.5 wt % GO in Figure 9(b),(c) show a much higher adhesion around the fiber surface. This indicates that a chemical bond between the modified carbon fibers and the modified matrix increased the epoxy adherence to the carbon fibers and formed a stronger interface. The fiber breakage also becomes more predominant, as shown in Figure 9(b),(c), instead of fiber pull-out or matrix debonding, as shown in Figure 9(a), indicating a higher interfacial strength on the modification of fiber and matrix. A more effective stress transfer between the fibers and the matrix due to a higher interfacial strength results in higher FS and ILSS values in modified laminates observed earlier.

The synergy of mechanical interlocking between CFs and the epoxy matrix provided by ZnO nanorods and the covalent interlinkage of BMI present on ZnO nanorods or ZnO nanorods and CF with the GO dispersed in the epoxy matrix could improve both FS and ILSS in s-BMI-ZnO−CFRE with 0.5 wt % GO and ns-BMI-ZnO−CFRE with 0.5 wt % GO, respectively. Furthermore, the enhancement in the surface area and segmental mobility in the BMI-modified systems helped induce better matrix adhesion and led to efficient self-healing. However, it seems that the thiol−ene click reaction route through which the s-BMI-ZnO−CFs were modified leaves intrinsic fiber damages and BMI is present only over ZnO nanorods, resulting in a lesser number of DA bonds in the case of s-CFs. These result in lower mechanical properties for s-BMI-ZnO−CFRE with 0.5 wt % GO as compared to ns-BMI-ZnO−CFRE with 0.5 wt % GO. However, the self-healing efficiency is higher for s-BMI-ZnO−CFRE with 0.5 wt % GO since its T_g value is close to the self-healing temperature, resulting in a higher molecular mobility and a higher proximity of BMI present on ZnO nanorods only with the GO present in the epoxy matrix, giving rise to a higher possibility of DA bond reformation. Figure 10 represents the various modes of interfacial strengthening in the modified laminates.

4.8. EMI Shielding. Electromagnetic interference (EMI) shielding is an important property to determine for composites applied to aircraft industries. The retardation and dissipation of incoming EM waves limit the malfunction of avionic equipment performance and ensure a safe and secure flight.[53,54]

The impact on EMI shielding performance due to interfacial modifications on the CFRE systems was evaluated in the X-band through a VNA instrument. Figure 11(a) shows the shielding effectiveness versus frequency curve for the various CFRE systems. It was observed that neat CFRE shows a total shielding efficiency (SE_T) of −38 dB, and the high SE_T value for neat CFRE can be attributed to the intrinsic high conductivity of the continuous bidirectional CF present in the composite, which induces conductive losses and attenuates the incoming EM waves. In addition to this, the conductivity mismatch between CF and epoxy results in charge accumulation at the interface resulting in interfacial polarization losses.[55−58]

In situ-grown ZnO−CFREs (Z-CFRE with 0.5 wt % GO) presented a SE_T value of −47 dB. The increase in SE can be attributed to the presence of GO and ZnO in the CFRE system. The nanoparticles, GO dispersed in the matrix, and ZnO attached to the CF surface form heterogeneous junctions in the CFRE. The conductivity mismatch at these sites induce charge accumulation and improve shielding performance by interfacial polarization. The functional groups present in GO can induce dipolar polarization losses and since ZnO is dielectric, it could also lead to EM attenuation through the dielectric polarization mechanism. The presence of ZnO nanorods connecting one CF mat with the other could augment the charge transfer between the laminae. Also, since ZnO is dielectric, it could lead to EM attenuation through the dielectric polarization mechanism. The percentage absorption−reflection (% SE_A and % SE_R) of the CFREs is presented in Figure 11(b). It can be seen that the dominant mechanism is predominantly absorption, and a slight increase in % SE_A can be noticed in the case of in situ-grown ZnO−CFREs (Z-CFRE with 0.5 wt % GO) due to the increased interfacial polarization and dielectric polarization mechanism.[59−61]
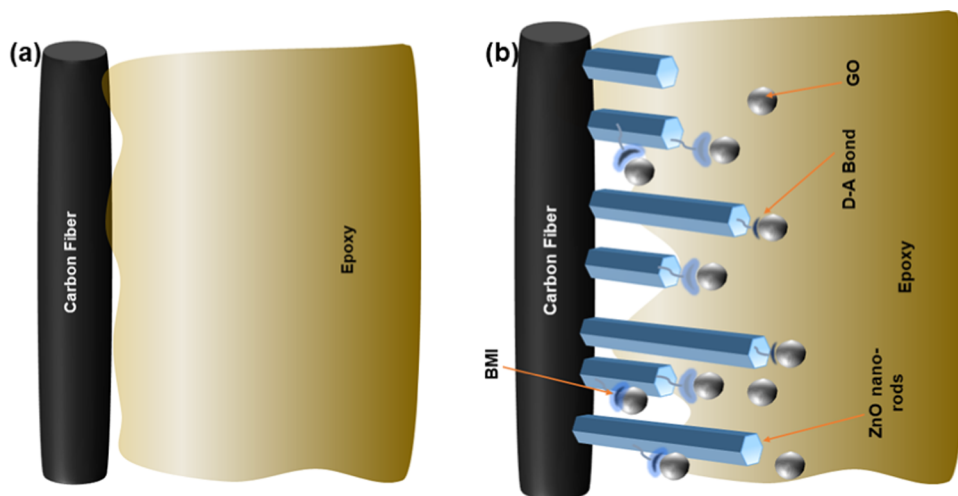
Figure 10. CF−epoxy interfacial scheme for (a) neat and (b) modified laminates with fiber and matrix modification.
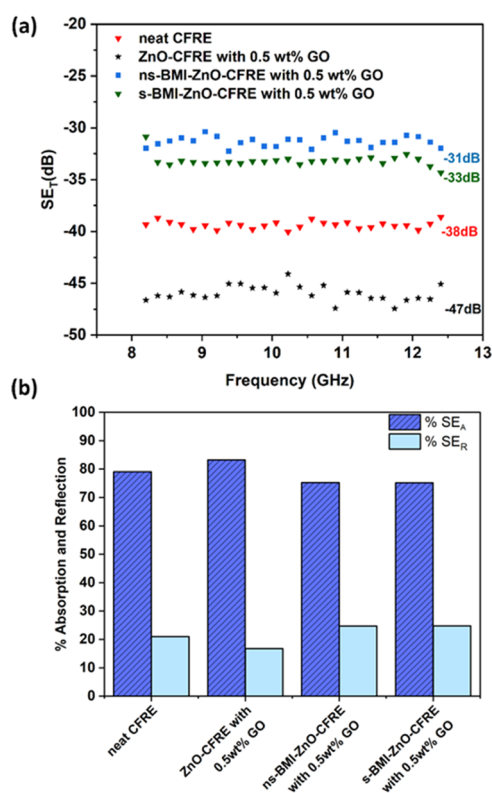

Figure 11. (a) Shielding effectiveness−frequency curve and (b) % absorption and reflection for neat CFRE, ZnO−CFRE with 0.5 wt % GO, ns-BMI-ZnO−CFRE with 0.5 wt % GO, and s-BMI-ZnO−CFRE with 0.5 wt % GO.

However, the addition of the BMI moiety on the surface of ZnO-grown CFs, both selectively or nonselectively, reduced the SE_T values of the resulting laminates, s-BMI-ZnO−CFRE with 0.5 wt % GO and ns-BMI-ZnO−CFRE with 0.5 wt % GO, to −33 and −31 dB, respectively. This deterioration in SE could be attributed to the hindrance in charge mobility between the subsequent CFs because of the BMI moiety.

5. CONCLUSIONS

In the present work, both carbon fibers (CFs) and the epoxy matrix were modified to improve the mechanical properties of the CFRE laminate by enhancing the interfacial strength. ZnO nanorods were grown in situ over CFs (ZnO−CF) through the SILAR technique. Deposition of BMI as the dienophile both selectively (s-BMI-ZnO−CF) and nonselectively (ns-BMI-ZnO−CF) over ZnO−CF was done through a covalent route. The deposition was done to achieve a synergistic improvement at the interface through mechanical impingement of the ZnO nanorods and thermo-reversible DA bonds formed by BMI with graphene oxide (GO) dispersed in the epoxy matrix. In s-BMI-ZnO−CF, BMI was observed to be deposited only over ZnO nanorods, whereas in ns-BMI-ZnO−CF, BMI was observed to be deposited both over ZnO nanorods and CF. GO also improved the strength of the epoxy matrix. Surface area and surface energy analyses on modified carbon fibers indicated an increase in the surface area generated due to higher defects and activated sites on CFs. Laminates were fabricated in both the cases of modified CFs, s-BMI-ZnO−CF, and ns-BMI-ZnO−CF, and the epoxy matrix having 0.5 wt % GO dispersed in it. Mechanical strength (FS and ILSS) of both the modified laminates was significantly increased with respect to the neat CFRE. The FS values of s-BMI-ZnO−CFRE with 0.5 wt % GO and ns-BMI_ZnO−CFRE with 0.5 wt % GO increased by 20 and 43%, respectively. Similarly, the ILSS values increased by 28 and 39%, respectively. The increase is due to the epoxy matrix being strengthened by the dispersion of GO in it and the fiber−matrix interface being strengthened by ZnO nanorods and BMI-GO DA bonds. It appears that the thiol−ene click chemistry through which s-BMI-ZnO−CF was treated adversely affected the fiber's intrinsic structural properties, making the mechanical properties of s-BMI-ZnO−CFRE with 0.5 wt % GO lower than those of ns-BMI-ZnO−CFRE.

The self-healing efficiency on ILSS samples, on the other hand, was 81% for s-BMI-ZnO−CFRE with 0.5 wt % GO and 73% for ns-BMI_ZnO−CFRE with 0.5 wt % GO. The strength recovery is attributed to the reformation of DA bonds at the interface with enhanced segmental motion through the lowering of Tg in the modified laminates, as observed from DMA. It appeared that the quantity of BMI interacting with the epoxy matrix was higher in the case of s-BMI-ZnO−CFRE as compared to that of ns-BMI-ZnO−CFRE, leading to a lower T_g value of the former. DMA also revealed an initial high elastic modulus for the modified laminates compared with the

neat CFRE. The initial higher stiffness of the modified laminates can be attributed to the fiber modifications that filled the spaces and cemented the warp and weft threads together.

SEM fractography of the fractured samples revealed a much better adhesion of epoxy around the fiber surface in the modified laminates as compared to the neat CFRE due to chemical bonds and a higher surface area. Hence, the failure mode predominantly became fiber fracture instead of fiber pull-out.

It was observed that BMI over the CF surface decreased the EMI shielding of the modified laminates by about 10 dB. This is because BMI hinders the conductivity at the interface.

Hierarchical CFRE laminate architectures having interfaces engineered with ZnO-based "zipped" interlocking and DA bond-based thermo-reversible interactions have not been reported to the best of our knowledge. A modified CF mat and epoxy matrix in the present work lead to a mechanical and chemical synergistic improvement in mechanical properties and strength recovery of the laminates.

■ ASSOCIATED CONTENT

⑤ Supporting Information

The Supporting Information is available free of charge at https://pubs.acs.org/doi/10.1021/acsomega.3c04728.

> Additional DMA data; loss modulus and tan delta plot of neat CFRE; ns-BMI-ZnO−CFRE with 0.5 wt % GO; and s-BMI-ZnO−CFRE with 0.5 wt % GO (PDF)

■ AUTHOR INFORMATION

Corresponding Author

Suryasarathi Bose − *Department of Materials Engineering, Indian Institute of Science, Bangalore 560012, India;* ⊙ orcid.org/0000-0001-8043-9192; Phone: +91-80-22933407; Email: sbose@iisc.ac.in

Authors

Poulami Banerjee − *Department of Materials Engineering, Indian Institute of Science, Bangalore 560012, India*

Sampath Parasuram − *Department of Materials Engineering, Indian Institute of Science, Bangalore 560012, India*

Subodh Kumar − *Department of Materials Engineering, Indian Institute of Science, Bangalore 560012, India*

Complete contact information is available at:
https://pubs.acs.org/10.1021/acsomega.3c04728

Author Contributions

[†]P.B. and S.P contributed equally.

Notes

The authors declare no competing financial interest.

■ ACKNOWLEDGMENTS

■ LIST OF ABBREVIATIONS

APTES	aminopropyltriethoxysilane
AFM	atomic force microscopy
BMI	bismaleimide
CF	carbon fiber
CFRE	carbon fiber-reinforced epoxy
CFRP	carbon fiber-reinforced polymer
DA	Diels−Alder
DMTA	dynamic mechanical thermal analysis
EMI	electromagnetic interference
EDX	energy-dispersive X-ray spectroscopy
EP	epoxy
FS	flexural strength
FTIR	fourier transform infrared spectroscopy
GO	graphene oxide
HMTA	hexamethylenetetramine
IR	infrared spectroscopy
IFSS	interfacial shear strength
ILSS	interlaminar shear strength
ns-BMI-ZnO−CF	nonselectively deposited BMI over ZnO−CF
s-BMI-ZnO−CF	selectively deposited BMI over ZnO−CF
SE	shielding effectiveness
SEM	scanning electron microscopy
SILAR	successive ionic layer adsorption and reaction
VARTM	vacuum assisted resin transfer molding
XRD	X-ray diffraction analysis
ZnO−CF	ZnO-modified CF

■ REFERENCES

(1) Mrázová, M. Advanced composite materials of the future in aerospace industry. *Incas Bulletin* **2013**, *5* (3), 139 DOI: 10.13111/2066-8201.2013.5.3.14.

(2) Kara, M.; Nomer, A. E.; Kepir, Y.; Gunoz, A.; Avci, A. Low-energy repeated impact response of nanoparticle reinforced carbon fiber epoxy composite pipes. *Compos. Struct.* **2022**, *299*, No. 116100, DOI: 10.1016/j.compstruct.2022.116100.

(3) Chen, Y.; Li, D.; Feng, S.; Huang, Q.; Chen, Z.; Shu, D. Optimization and thermal-performance deep learning on carbon/epoxy composite panels with microchannel structure for battery cooling. *Appl. Thermal Eng.* **2022**, *217*, No. 119162.

(4) Abd Hamid, A. R.; Chin, T. M. Design and Analysis of Composite Materials for Vehicle Engine Mount. In *Technological Advancement in Mechanical and Automotive Engineering: Proceeding of International Conference in Mechanical Engineering Research*; Springer Nature Singapore: Singapore, 2021; pp 121−132.

(5) Regassa, Y.; Gari, J.; Lemu, H. G. Composite Overwrapped Pressure Vessel Design Optimization Using Numerical Method. *J. Compos. Sci.* **2022**, *6* (8), 229.

(6) Bandegi, A.; Montemayor, M.; Manas-Zloczower, I. Vitrimerization of rigid thermoset polyurethane foams: A mechanochemical method to recycle and reprocess thermosets. *Poly. Adv. Technol.* **2022**, *33* (10), 3750−3758, DOI: 10.1002/pat.5827.

(7) Wu, Y.; Jiao, Y.; Rong, Z.; Gao, C.; Liu, Y. Reprocessable thermoset organosilicon elastomer with good self-healable and high stretchable properties for flexible electronic devices. *Polym. Degrad. Stab.* **2022**, *204*, No. 110110.

(8) Hong, Y.; Jeong, J.; Oh, D.; Kim, M.; Lee, M. W.; Goh, M. On-demand and fast recyclable bio-epoxy. *J. Ind. Eng. Chem.* **2023**, *117*, 490−499.

(9) Chen, Y.; Wu, Y.; Zhao, W. Constructing Ti3C2Tx/Carbon fiber hybrids for enhancing the interfacial strength and erosion wear resistance of EP-based composite coating. *Carbon* **2023**, *202*, 196−206.

(10) Zhou, Z.; Zheng, N.; Sun, W. Self-interlocked MXene/polyvinyl alcohol aerogel network to enhance interlaminar fracture toughness of carbon fibre/epoxy composites. *Carbon* **2023**, *201*, 60−70.

(11) Jones, A. R.; Cintora, A.; White, S. R.; Sottos, N. R. Autonomic healing of carbon fiber/epoxy interfaces. *ACS Appl. Mater. Interfaces* **2014**, *6* (9), 6033−6039.

(12) Chen, X.; Wen, K.; Wang, C.; Cheng, S.; Wang, S.; Ma, H.; Tian, H.; Zhang, J.; Li, X.; Shao, J. Enhancing mechanical strength of carbon fiber-epoxy interface through electrowetting of fiber surface. *Composites, Part B* **2022**, *234*, No. 109751.

(13) Biro, D. A.; McLean, P.; Deslandes, Y. Application of the microbond technique: Characterization of carbon fiber-epoxy interfaces. *Polym. Eng. Sci.* **1991**, *31* (17), 1250−1256.

(14) Zhu, S.; Shi, R.; Qu, M.; Zhou, J.; Ye, C.; Zhang, L.; Cao, H.; Ge, D.; Chen, Q. Simultaneously improved mechanical and electromagnetic interference shielding properties of carbon fiber fabrics/epoxy composites via interface engineering. *Compos. Sci. Technol.* **2021**, *207*, No. 108696.

(15) Qiu, B.; Zhang, X.; Xia, S.; Sun, T.; Ling, Y.; Zhou, S.; Guang, H.; et al. Magnetic graphene oxide/carbon fiber composites with improved interfacial properties and electromagnetic interference shielding performance. *Composites, Part A* **2022**, *155*, No. 106811, DOI: 10.1016/j.compositesa.2022.106811.

(16) Banerjee, P.; Bhattacharjee, Y.; Bose, S. Lightweight epoxy-based composites for EMI shielding applications. *J. Electron. Mater.* **2020**, *49*, 1702−1720.

(17) Han, S.; Chung, D. D. L. Strengthening and stiffening carbon fiber epoxy composites by halloysite nanotubes, carbon nanotubes and silicon carbide whiskers. *Appl. Clay Sci.* **2013**, *83-84*, 375−382.

(18) Wang, J.; Zhang, X.; Miao, Y.; Li, Y.; Xi, X.; Zhong, X.; Pei, X.; He, L.; Huang, Q. The influences of carbon nanotubes introduced in three different phases of carbon fiber/pyrolytic carbon/silicon carbide composites on microstructure and properties of their composites. *Carbon* **2018**, *129*, 409−414.

(19) Bhanuprakash, L.; Parasuram, S.; Varghese, S. Experimental investigation on graphene oxides coated carbon fibre/epoxy hybrid composites: Mechanical and electrical properties. *Compos. Sci. Technol.* **2019**, *179*, 134−144.

(20) Parasuram, S.; Banerjee, P.; Raj, R.; Kumar, S.; Bose, S. Electrophoretically Deposited Multiscale Graphene Oxide/Carbon Nanotube Construct Mediated Interfacial Engineering in Carbon Fiber Epoxy Composites. *ACS Appl. Mater. Interfaces* **2023**, *15*, 28581−28593, DOI: 10.1021/acsami.3c04538.

(21) Ghasemi, A. R.; Mohandes, M.; Dimitri, R.; Tornabene, F. Agglomeration effects on the vibrations of CNTs/fiber/polymer/metal hybrid laminates cylindrical shell. *Composites, Part B* **2019**, *167*, 700−716.

(22) Reale Batista, M. D.; Drzal, L. T. Carbon fiber/epoxy matrix composite interphases modified with cellulose nanocrystals. *Compos. Sci. Technol.* **2018**, *164*, 274−281.

(23) Ma, L.; Zhu, Y.; Feng, P.; Song, G.; Huang, Y.; Liu, H.; Zhang, J.; Fan, J.; Hou, H.; Guo, Z. Reinforcing carbon fiber epoxy composites with triazine derivatives functionalized graphene oxide modified sizing agent. *Composites, Part B* **2019**, *176*, No. 107078.

(24) Banerjee, P.; Kumar, S.; Bose, S. Thermoreversible bonds and graphene oxide additives enhance the flexural and interlaminar shear strength of self-healing epoxy/carbon fiber laminates. *ACS Appl. Nano Mater.* **2021**, *4* (7), 6821−6831.

(25) Banerjee, P.; Parasuram, S.; Kumar, S.; Bose, S. Graphene oxide-mediated thermo-reversible bonds and in situ grown nano-rods trigger 'self-healable' interfaces in carbon fiber laminates. *Nanoscale* **2022**, *14* (25), 9004−9020.

(26) Yasuda, K.; Sugane, K.; Shibata, M. Self-healing high-performance thermosets utilizing the furan/maleimide Diels-Alder and amine/maleimide Michael reactions. *J. Polym. Res.* **2020**, *27* (1), 18.

(27) Hoyle, C. E.; Bowman, C. N. Thiol−ene click chemistry. *Angew. Chem., Int. Ed.* **2010**, *49* (9), 1540−1573.

(28) Goren, A.; Atas, C. Manufacturing of polymer matrix composites using vacuum assisted resin infusion molding. *Arch. Mater. Sci. Eng.* **2008**, *34* (2), 117−120.

(29) Rouhi, M. S.; et al. Effects of manufacturing on the structural performance of composites in vacuum assisted resin transfer molding. *J. Reinf. Plast. Compos.* **2023**, *42* (5-6), 264−278, DOI: 10.1177/07316844221118691.

(30) Guo, S.; Garaj, S.; Bianco, A.; Ménard-Moyon, C. Controlling covalent chemistry on graphene oxide. *Nat. Rev. Phys.* **2022**, *4* (4), 247−262.

(31) Brisebois, P. P.; Kuss, C.; Schougaard, S. B.; Izquierdo, R.; Siaj, M. New insights into the Diels−Alder reaction of graphene oxide. *Chem. −Eur. J.* **2016**, *22* (17), 5849−5852.

(32) Dai, Z.; Zhang, B.; Shi, F.; Li, M.; Zhang, Z.; Gu, Y. Effect of heat treatment on carbon fiber surface properties and fibers/epoxy interfacial adhesion. *Appl. Surf. Sci.* **2011**, *257* (20), 8457−8461.

(33) Dilsiz, N.; Wightman, J. P. Surface analysis of unsized and sized carbon fibers. *Carbon* **1999**, *37* (7), 1105−1114.

(34) Dynes, P. J.; Kaelble, D. H. Surface energy analysis of carbon fibers and films. *J. Adhes.* **1974**, *6* (3), 195−206.

(35) Washer, G.; Blum, F. Raman spectroscopy for the non-destructive testing of carbon fiber. *Res. Lett. Mater. Sci.* **2008**, *2008*, No. 693207, DOI: 10.1155/2008/693207.

(36) Paillet, M.; Parret, R.; Sauvajol, J.-L.; Colomban, P. Graphene and related 2D materials: An overview of the Raman studies. *J. Raman Spectrosc.* **2018**, *49* (1), 8−12.

(37) Feng, P.; Song, G.; Li, X.; Xu, H.; Xu, L.; Lv, D.; Zhu, X.; Huang, Y.; Ma, L. Effects of different "rigid-flexible" structures of carbon fibers surface on the interfacial microstructure and mechanical properties of carbon fiber/epoxy resin composites. *J. Colloid Interface Sci.* **2021**, *583*, 13−23.

(38) Lu, J.; Li, W.; Kang, H.; Feng, L.; Xu, J.; Liu, R. Microstructure and properties of polyacrylonitrile based carbon fibers. *Polym. Test.* **2020**, *81*, No. 106267.

(39) Zeng, L.; Liu, X.; Chen, X.; Soutis, C. π-π interaction between carbon fibre and epoxy resin for interface improvement in composites. *Composites, Part B* **2021**, *220*, No. 108983.

(40) Zakaria, M. R.; Akil, H. M.; Omar, M. F.; Abdullah, M. M. A. B.; Rahman, A. A. A.; Othman, M. B. H. Improving flexural and dielectric properties of carbon fiber epoxy composite laminates reinforced with carbon nanotubes interlayer using electrospray deposition. *Nanotechnol. Rev.* **2020**, *9* (1), 1170−1182.

(41) Yuan, X.; Zhu, B.; Cai, X.; Qiao, K.; Zhao, S.; Yu, J. Influence of different surface treatments on the interfacial adhesion of graphene oxide/carbon fiber/epoxy composites. *Appl. Surf. Sci.* **2018**, *458*, 996−1005.

(42) Zheng, N.; He, J.; Gao, J.; Huang, Y.; Besenbacher, F.; Dong, M. Adhesion force measured by atomic force microscopy for direct carbon fiber-epoxy interfacial characterization. *Mater. Des.* **2018**, *145*, 218−225.

(43) Schneck, T. K.; Brück, B.; Schulz, M.; Spörl, J. M.; Hermanutz, F.; Clauß, B.; Mueller, W. M.; et al. Carbon fiber surface modification for tailored fiber-matrix adhesion in the manufacture of C/C-SiC composites. *Composites, Part A* **2019**, *120*, 64−72, DOI: 10.1016/j.compositesa.2019.02.021.

(44) Xiao, C.; Tan, Y.; Wang, X.; Gao, L.; Wang, L.; Qi, Z. Study on interfacial and mechanical improvement of carbon fiber/epoxy composites by depositing multi-walled carbon nanotubes on fibers. *Chem. Phys. Lett.* **2018**, *703*, 8−16.

(45) Thomsen, H.; Spacone, E.; Limkatanyu, S.; Camata, G. Failure mode analyses of reinforced concrete beams strengthened in flexure with externally bonded fiber-reinforced polymers. *J. Compos. Constr.* **2004**, *8* (2), 123−131, DOI: 10.1061/(ASCE)1090-0268(2004)8:2(123).

(46) Siddika, A.; Mamun, M. A. A.; Alyousef, R.; Amran, Y. H. M. Strengthening of reinforced concrete beams by using fiber-reinforced polymer composites: A review. *J. Build. Eng.* **2019**, *25*, No. 100798.

(47) Sethi, S.; Rathore, D. K.; Ray, B. C. Effects of temperature and loading speed on interface-dominated strength in fibre/polymer

composites: An evaluation for in-situ environment. *Mater. Des. (1980−2015)* **2015**, *65*, 617−626.

(48) Akay, M.; Spratt, G. R.; Meenan, B. The effects of long-term exposure to high temperatures on the ILSS and impact performance of carbon fibre reinforced bismaleimide. *Compos. Sci. Technol.* **2003**, *63* (7), 1053−1059.

(49) Dong, S.; Gauvin, R. Application of dynamic mechanical analysis for the study of the interfacial region in carbon fiber/epoxy composite materials. *Polym. Compos.* **1993**, *14* (5), 414−420.

(50) ElFaham, M. M.; Mostafa, A. M.; Nasr, G. M. Unmanned aerial vehicle (UAV) manufacturing materials: Synthesis, spectroscopic characterization and dynamic mechanical analysis (DMA). *J. Mol. Struct.* **2020**, *1201*, No. 127211.

(51) Chen, Y.; Lloyd, D. W.; Harlock, S. C. Mechanical characteristics of coated fabrics. *J. Text. Inst.* **1995**, *86* (4), 690−700, DOI: 10.1080/00405009508659045.

(52) Moaseri, E.; Maghrebi, M.; Baniadam, M. Improvements in mechanical properties of carbon fiber-reinforced epoxy composites: a microwave-assisted approach in functionalization of carbon fiber via diamines. *Mater. Design* **2014**, *55*, 644−652, DOI: 10.1016/j.matdes.2013.10.040.

(53) Luo, X.; Chung, D. D. L. Electromagnetic interference shielding using continuous carbon-fiber carbon-matrix and polymer-matrix composites. *Composites, Part B* **1999**, *30* (3), 227−231.

(54) Raj, R.; Parasuram, S.; Kumar, S.; Bose, S. Process dependent interface strengthening, de-icing and EMI shielding performance in PEEK/CF laminates. *Mater. Adv.* **2023**, *4*, 4180−4189.

(55) Gupta, S.; Tai, N.-H. Carbon materials and their composites for electromagnetic interference shielding effectiveness in X-band. *Carbon* **2019**, *152*, 159−187.

(56) Singh, A. K.; Kumar, A.; Srivastava, A.; Yadav, A. N.; Haldar, K.; Gupta, V.; Singh, K. Lightweight reduced graphene oxide-ZnO nanocomposite for enhanced dielectric loss and excellent electromagnetic interference shielding. *Composites, Part B* **2019**, *172*, 234−242, DOI: 10.1016/j.compositesb.2019.05.062.

(57) Shayesteh Zeraati, A.; Sundararaj, U. Carbon nanotube/ZnO nanowire/polyvinylidene fluoride hybrid nanocomposites for enhanced electromagnetic interference shielding. *Can. J. Chem. Eng.* **2020**, *98* (5), 1036−1046.

(58) Sushmita, K. Multi-layered Composite Structures for Electromagnetic Interference Shielding Applications, Doctoral dissertation; 2022.

(59) Sushmita, K.; Ghosh, D.; Nilawar, S.; Bose, S. Absorption Dominated Directional Electromagnetic Interference Shielding through Asymmetry in a Multilayered Construct with an Exceptionally High Green Index. *ACS Appl. Mater. Interfaces* **2022**, *14* (43), 49140−49157.

(60) Rohini, R.; Bose, S. Electrodeposited carbon fiber and epoxy based sandwich architectures suppress electromagnetic radiation by absorption. *Composites, Part B* **2019**, *161*, 578−585.

(61) Singh, S. K.; Akhtar, M. J.; Kar, K. K. Hierarchical carbon nanotube-coated carbon fiber: ultra lightweight, thin, and highly efficient microwave absorber. *ACS Appl. Mater. Interfaces* **2018**, *10* (29), 24816−24828, DOI: 10.1021/acsami.8b06673.